Bioactive Materials 35 (2024) 228–241

Contents lists available at ScienceDirect

Bioactive Materials

journal homepage: www.keaipublishing.com/en/journals/bioactive-materials

Reversing cancer immunoediting phases with a tumor-activated and optically reinforced immunoscaffold

Xinchao Li [a,1], Xiuqi Liang [a,1], Wangxian Fu [a], Rui Luo [a], Miaomiao Zhang [a], Xiaorong Kou [a], Yi Zhang [b], Yingjie Li [a], Dongxue Huang [a], Yanjie You [c], Qinjie Wu [a,**], Changyang Gong [a,*]

[a] Department of Biotherapy, Cancer Center and State Key Laboratory of Biotherapy, West China Hospital, Sichuan University, Chengdu, 610041, China
[b] Department of Anesthesiology, Shengjing Hospital of China Medical University, Shenyang, 110022, China
[c] Department of Gastroenterology, People's Hospital of Ningxia Hui Autonomous Region, Yinchuan, 750002, China

ARTICLE INFO

Keywords:
Hydrogel
Immunoscaffold
In situ vaccine
Photothermal therapy
Immunoediting phases

ABSTRACT

In situ vaccine (ISV) is a promising immunotherapeutic tactic due to its complete tumoral antigenic repertoire. However, its efficiency is limited by extrinsic inevitable immunosuppression and intrinsic immunogenicity scarcity. To break this plight, a tumor-activated and optically reinforced immunoscaffold (TURN) is exploited to trigger cancer immunoediting phases regression, thus levering potent systemic antitumor immune responses. Upon response to tumoral reactive oxygen species, TURN will first release RGX-104 to attenuate excessive immunosuppressive cells and cytokines, and thus immunosuppression falls and immunogenicity rises. Subsequently, intermittent laser irradiation-activated photothermal agents (PL) trigger abundant tumor antigens exposure, which causes immunogenicity springs and preliminary infiltration of T cells. Finally, CD137 agonists from TURN further promotes the proliferation, function, and survival of T cells for durable antitumor effects. Therefore, cancer immunoediting phases reverse and systemic antitumor immune responses occur. TURN achieves over 90 % tumor growth inhibition in both primary and secondary tumor lesions, induces potent systemic immune responses, and triggers superior long-term immune memory *in vivo*. Taken together, TURN provides a prospective sight for ISV from the perspective of immunoediting phases.

1. Introduction

In situ vaccine (ISV) is an emerging immunotherapeutic tactic owing to it can induce complete tumoral antigen exposure, including the evolving tumor antigen arrays, to amplify and broaden antigen-specific T cells [1–4]. Attributed to tumor-infiltrating DCs uptake of tumor antigens from dying tumor cells, ISV could construct *in situ* tumor antigen repository in the tumor microenvironment (TME) itself rather than selecting, purifying, and preparing, thus provoking an adaptive immune response [5,6]. ISV was highly expected to achieve effective tumor growth control, tumor progress regression, and even tumor lesion elimination. However, it was submitted to multiple resistance inevitably when the tumor became visible, which meant the immunoediting phases had deteriorated from "elimination" or "equilibrium" to "escape" [7–11].

The "escape" immunoediting phase was composed of the combination of the extrinsic mechanism, immunosuppression triggered severe T cell dysfunction, and the intrinsic mechanism, low immunogenicity induced scarce T cell infiltration. In detail, the extrinsic tumor immunosuppressive microenvironment, including immunosuppressive cells and cytokines, would promote tumor growth out of control and lead to the silence of the immune system. It had been reported that regulating the proportion or function of myeloid-derived suppressor cells (MDSCs), tumor-associated macrophages (TAM), and regulatory T cells (Tregs) could contribute to immunosuppression amelioration and tumor burden remission [12–16]. Liver-X nuclear hormone receptors (LXRα and LXRβ) agonists have been reported to activate the LXR/ApoE axis to inhibit the survival of MDSCs and reduce their abundance [17]. As an effective LXR-β agonist, the application of RGX-104 on MDSCs might represent a practical strategy for immunosuppression relief. However,

Peer review under responsibility of KeAi Communications Co., Ltd.
* Corresponding author.
** Corresponding author.
E-mail addresses: cellwqj@scu.edu.cn (Q. Wu), gongchangyang@scu.edu.cn (C. Gong).
[1] These authors contributed equally to this work.

https://doi.org/10.1016/j.bioactmat.2024.01.026
Received 16 October 2023; Received in revised form 19 January 2024; Accepted 30 January 2024

immunosuppression amelioration alone was difficult to eliminate tumor lesions due to tumor antigens scarcity.

The intrinsic scarcity of tumor antigens led to poor tumor recognition and cytotoxicity of T cells. Recently, radiotherapy [18,19], chemotherapy [20,21], and phototherapy [22–25] have been reported to promote tumor antigen exposure in TME, thus improving the immunogenicity of ISV. Among them, photothermal therapy (PTT) has emerged as a novel ISV paradigm due to its high selectivity, low systemic toxicity, and limited therapeutic resistance [26–29]. In addition, the local heat of tumor lesions could accelerate blood flow, increase vascular permeability, and relieve interstitial pressure to facilitate the preliminary infiltration of T cells [30]. Effective PTT was dependent on the photothermal agents with superior photothermal conversion ability and photothermal stability. As a natural melanin analog, polydopamine nanoparticles (PDA Nps) exhibited superior biodegradability and good biocompatibility, which endowed its potential application in organisms [31]. In addition, hydrophilic PDA Nps displayed effective photothermal conversion ability and excellent photothermal stability upon near-infrared (NIR) irradiation, which allowed it wide exploration in photothermal therapy [32]. Finally, PDA Nps could be prepared by simple self-polymerization with alkaline water, which facilitated industrial production [33]. However, the exposure of tumor antigens after PTT was insufficient of inducing a potent and durable systemic immune response for minimal tumor residues or tumor elimination [34]. Potent and durable systemic immune responses relied on the extensive infiltration, potent effector function, and durable viability of cytotoxic T cells to initiate the formation of pivotal antitumor immune memory. Direct T cells agonists, such as CD137 agonists, might provide a potential strategy to achieve those goals. CD137, a member of the tumor necrosis factor receptor superfamily, was mainly expressed on $CD4^+$ and $CD8^+$ T cells as a significant co-stimulatory factor for powerful T cell proliferation, activation, effector function, and survival [35,36]. However, it would cause hepatotoxicity when administered systemically, which supported the imminence of local CD137 agonists administration for sustained release [37].

Herein, we exploited a tumor-activated and optically reinforced immunoscaffold (TURN) to trigger local cancer immunoediting phases regression and lever a potent systemic antitumor immune response (Fig. 1A and B). It will unshackle extrinsic inevitable immunosuppression steadily and improve intrinsic immunogenicity scarcity stepwise, which could evoke a sequentially enhanced cascade amplification of T cells-dependent antitumor effects to reverse "escape" immunoediting phases to "equilibrium", or further to "elimination" with single TURN administration (Fig. 1C). In detail, upon being responsive to reactive oxygen species (ROS), TURN would first release RGX-104 that induced a decline of immunosuppressive cells (MDSCs, *etc.*) and cytokines (IL-10, *etc.*) to mitigate the extrinsic obstacle of ISV [38]. The relief of immunosuppression would convert immunoediting phases from "escape" to

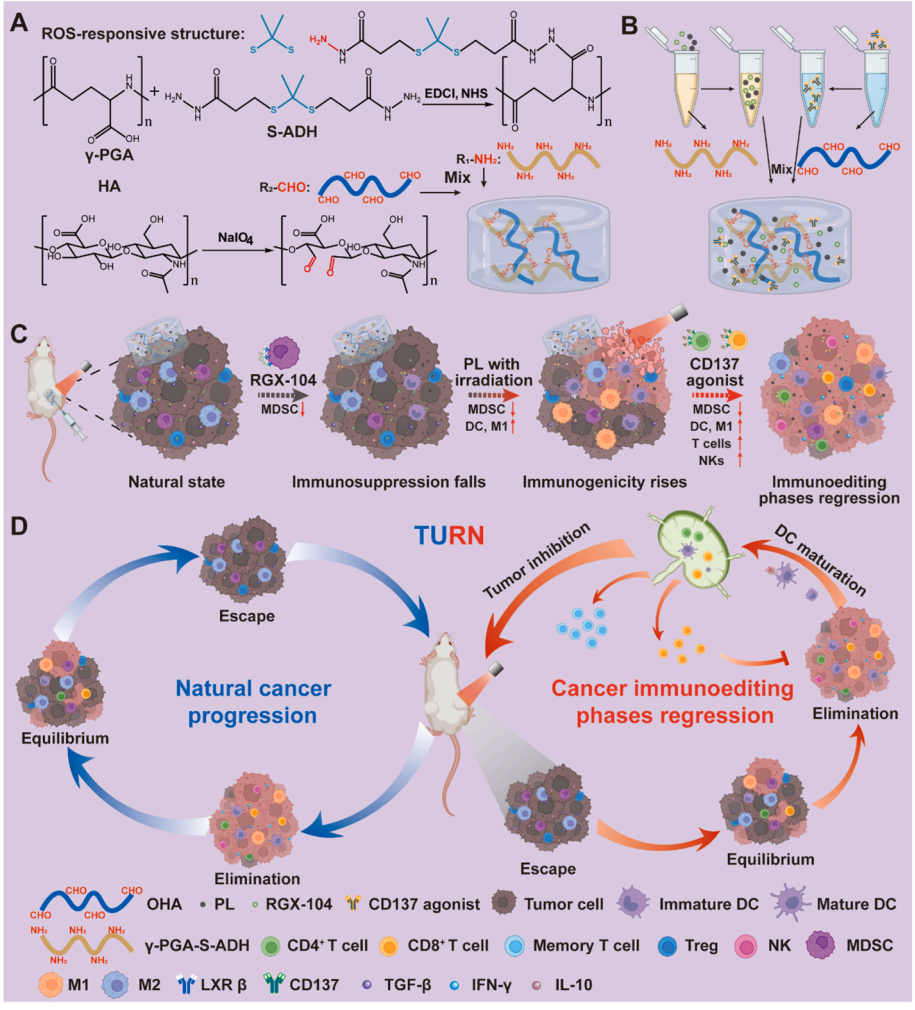

Fig. 1. TURN triggered local cancer immunoediting phases regression and levered a potent systemic antitumor immune response. A) Chemical structures and synthetic routes of the hydrogel scaffold matrix, OHA and γPGA-S-ADH. B) Compositions and preparation of TURN. C) The concrete working principle of TURN to reverse cancer immunoediting phases. D) The cancer immunoediting phases progress with or without TURN treatment. Source materials of scheme illustration come from the website of app.Biorender.com.

"equilibrium", thus paving the way for the following "elimination" through immunogenicity improvement. Subsequently, the accumulated photothermal agents (phase change materials coated polydopamine nanoparticles) were ignited by laser irradiation to induce tumor cell death and trigger abundant tumor antigens release stepwise for immunogenicity improvement, which would prompt tumor-infiltrating DCs to recruit T cells spontaneously for launching an adaptive immune response. Finally, CD137 agonists released from TURN would further promote the proliferation, survival, and function of tumor-infiltrating T cells [39,40]. Profited from continuously removing the extrinsic obstacle and termly unshackling the intrinsic obstacle, TURN reversed local tumor immunoediting phases, launched a systemic antitumor immune response, and initiated long-term immune memory (Fig. 1D). Taken together, TURN was a broad-spectrum vaccine tactic with prospect and provided a novel sight for ISV from the perspective of immunoediting phases regression.

2. Results and discussion

2.1. Preparation and characterization of the long-term photothermal agent repository

Polydopamine nanoparticles (PDA NPS) were coated with phase change materials to obtain PL NPS, which avoided them being degraded in a hydrogen peroxide (H_2O_2) environment and had no impact on their photothermal conversion ability. In brief, PDA NPS were prepared via auto polymerization of dopamine in an alkalescent Ethanol-Water solution [41], whose average hydrodynamic dimension was 120.1 ± 1.8 nm (PdI: 0.113 ± 0.013). The spherical uniform morphologies of PDA NPS were observed by transmission electron microscope (TEM)

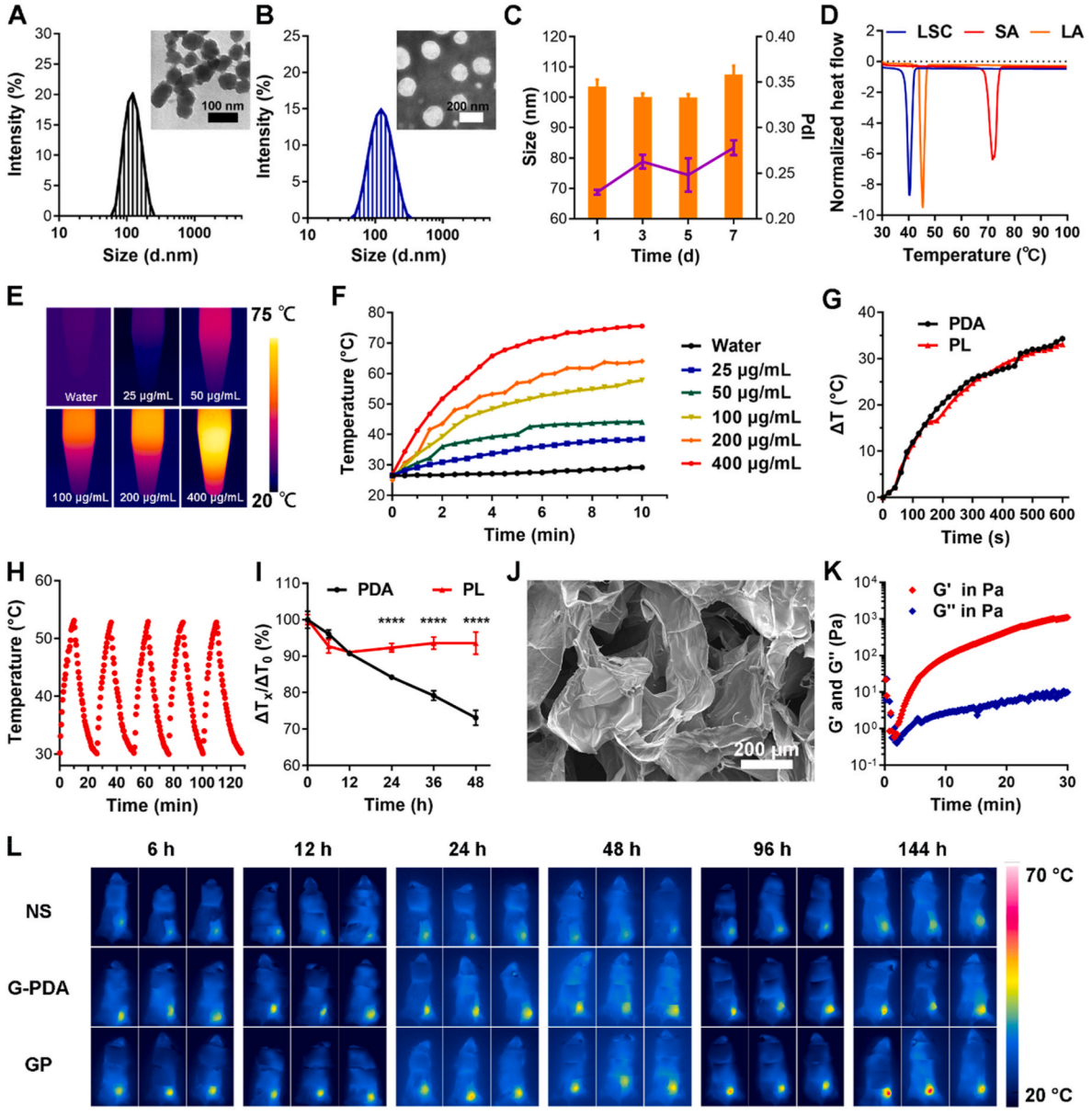

Fig. 2. Characterization of the long-term photothermal agent repository. Size distribution and TEM images of A) PDA NPS and B) PL NPS. Scale bars, 200 nm. C) Size stability test of PL NPS within one week. D) DSC heat curves of LA, SA, and LSC. E) Thermal images and F) Temperature change curves of PL NPS at various concentrations (0, 25, 50, 100, 200, 400 μg/mL) under 808 nm laser (2 W/cm^2) for 10 min. G) Temperature change curves of PDA and PL NPS at 100 μg/mL under 808 nm laser (2 W/cm^2) for 10 min. H) On-off cycles of PL NPS. I) Temperature change ratios of PDA and PL NPS after being treated with hydrogen dioxide (5 μM) at different times. J) SEM image of PL-loaded hydrogel. K) Rheological properties of PL-loaded hydrogel. L) Photothermal effect of NS, G-PDA, and GP *in vivo*. (Data are presented as mean ± SD, $*p < 0.05$, $**p < 0.01$, $***p < 0.001$, $****p < 0.0001$).

(Fig. 2A). PL NPS were obtained by wrapping PDA with a mixture of lauric acid (LA), stearic acid (SA), lecithin, and DSPE-mPEG2000. The size distribution of PL NPS was 181.0 ± 2.5 nm (PdI: 0.292 ± 0.010) (Fig. 2B). Subsequently, the stabilities of PL NPS in PBS were detected periodically. Results showed that PL NPS were still around 200 nm, which meant they were stable for at least one week (Fig. 2C).

The differential scanning calorimetry (DSC) heat curve showed that the peak melting temperature of LA and SA was 44.7 °C and 70.4 °C, respectively. The eutectic crystal of LA and SA displayed a lower peak melting temperature, which was 40.6 °C (Fig. 2D). Subsequently, we investigated the photothermal effect of PL NPS with different concentrations (0, 25, 50, 100, 200, and 400 μg/mL). They were irradiated with an 808 nm laser (2 W/cm^2, 10 min) and detected by an infrared thermal imaging camera. The images and temperature change curves of PL NPS (Fig. 2E and F) showed their concentration-dependent photothermal conversion capacities. The photothermal conversion abilities of PDA and PL NPS (100 μg/mL) were explored next and they had no statistical differences as shown in Fig. 2G, which meant the coats would have no impact on the photothermal effect of PDA. Five on-off processes were performed to determine the thermal stability of PL NPS at 100 μg/mL (Fig. 2H and Fig. S1). The parallel maximal temperature change and temperature change rate of five cycles indicated their outstanding thermal stabilities. Former studies showed that PDA NPS could be degraded by tumoral abundant H_2O_2, which might hinder their retention at the tumor site for photothermal conversion performance [41,42]. Therefore, we explored whether the degradation of PL NPS could be decelerated in H_2O_2. PDA and PL NPS (100 μg/mL) were stirred with H_2O_2 (5 mM) separately for 24 h. The image exhibited PDA NPS would form sedimentation on the bottom (Fig. S2). Moreover, PDA NPS displayed a lighter color than PL NPS after shaking. Subsequently, we examined the photothermal conversion effect of PDA and PL NPS after being treated with H_2O_2 (5 mM). The ratio of the temperature change of sometime (ΔT_x) to that of 0 h (ΔT_0) was utilized to evaluate the H_2O_2-induced change of the photothermal conversion effect. The specific value of PDA NPS was down to nearly 70 % while that of PL NPS was still more than 90 %, which supported the coats could decelerate the degradation of PDA NPS (Fig. 2I).

To construct a long-term photothermal agent repository with only one administration, a hydrogel was synthesized and prepared as in previous studies [43]. The image of hydrogel and PL-loaded hydrogel was shown in Fig. S3. The scanning electron microscope described the loose porous structure of PL-loaded hydrogel (Fig. 2J). Additionally, rheological characteristics of hydrogel and PL-loaded hydrogel were assessed by detecting storage modulus G′ and loss modulus G″ in Fig. 2K and Fig. S4. Hydrogel loaded with PL didn't affect its gelation time.

To verify the retention of the long-term photothermal agent repository *in vivo*, the hydrogel was implanted subcutaneously in BALB/c mice to evaluate its degradation behavior. There was still an apparent hydrogel boundary at the injection site 7 days post-injection. Furthermore, hydrogel residue could also be observed on the 14th day (Fig. S5), which indicated the hydrogel had a durable degradation period. In addition, normal saline (NS), PDA-loaded hydrogel (G-PDA), or PL-loaded hydrogel (GP) was injected peritumorally in 4T1 tumor-bearing mice to monitor their photothermal conversion capacities via photothermal imaging *in vivo* [44]. There was almost no temperature change in NS while mice of G-PDA and GP exhibited temperature rise after administration (Fig. 2L). Consistent with what had been detected in H_2O_2 *in vitro*, the temperature of GP raised higher than that of G-PDA at 96 h and 144 h, which might be due to the excellent H_2O_2 tolerance ability of PL.

Stimulus-activated drug delivery systems have prevailed in designing safer, more precise, and more intelligent drug carriers for better realization of tumor therapies [45,46]. To evaluate the ROS-responsive drug release of the hydrogel scaffold, RGX-104 and BSA-FITC (a model protein) were both loaded into the hydrogel and shaken in PBS with or without 1 mM H_2O_2 at 37 °C, 90 rpm for 144 h. As shown in Fig. S6, the release rate of RGX-104 was 23.31 % ± 3.66 % when the scaffold was shaken at PBS for 96 h, while it reached 91.93 % ± 0.59 % when the scaffold was shaken at PBS containing 1 mM H_2O_2 over the same period, which suggested the rapid release of RGX-104 from the scaffold under high redox conditions. The release profile of BSA-FITC exhibited the same trend as that of RGX-104. In detail, the release rate of BSA-FITC was over 90 % in PBS for 120 h, while it was lower than 20 % in PBS containing 1 mM H_2O_2 (Fig. S7). These data proved the tumor ROS-activated release behavior of the scaffold. In addition, the release rate of RGX-104 from the scaffold was over 50 % within 24 h while BSA-FITC required more than 48 h to achieve 50 %, which indicated the hydrogel scaffold enabled the cascade release of different cargoes.

2.2. TURN promoted DCs maturation and MDSCs decline in vitro

Cell viabilities of PDA and PL NPS on 4T1 cells were evaluated by MTT assay (Figs. S8 and 9). The cell viability remained about 90 % when 4T1 cells were incubated with PL NPS at 200 μg/mL without laser, while it was lower than 60 % when 4T1 cells were treated with PDA NPS. Additionally, the cell viabilities of PDA and PL NPS on CT26 cells were also detected (Fig. S10). Subsequently, we explored whether PL NPS could induce 4T1 apoptosis *in vitro* (Fig. 3A). The apoptosis ratios of 4T1 co-incubated with free medium and PL NPS were both about 9 % while that of PL NPS raised to 40 % after irradiation (Fig. 3B).

Utilizing RGX-104 *in vitro*, we found it could regulate MDSCs abundance, similar to reported before [17,38]. In brief, 4T1 cells and MDSCs were treated with a concentration gradient of RGX-104, respectively. RGX-104 showed just modest toxicity to 4T1 at 4 μM (Fig. S11) while it could significantly reduce the ratio of MDSCs, which represented its excellent inhibition of MDSCs (Fig. 3C and D).

To explore whether the function of CD137 agonists would be impaired upon laser irradiation, splenic T cells were separated and cultured with CD137 agonists or heat-pretreated CD137 agonists (42 °C, 10 min) for 72 h. Subsequently, the memory, early activation, and effector function of splenic T cells were measured by flow cytometry. CD137 agonists and heat-pretreated CD137 agonists both improved the proportions of $CD44^+CD4^+$ (Fig. S12A) and $CD44^+CD8^+$ (Fig. S12B) memory T cells when compared with the control group. The results in Figs. S12C and D demonstrated that CD137 agonists could effectively improve the early activation of $CD4^+$ T cells (CD137 agonists vs NS: 38.18 % ± 1.77 % vs 79.26 % ± 1.52 %) and $CD8^+$ T cells (CD137 agonists vs NS: 34.60 % ± 1.27 % vs 51.39 % ± 1.60 %). There were negligible differences between CD137 agonists and heat-pretreated CD137 agonists. Finally, the effector function of T cells was evaluated with the proportion of IFN-γ^+ T cells (Figs. S12E and F). Compared to the control group, both CD137 agonists and heat-pretreated CD137 agonists exhibit similar improvement of $CD8^+$IFN-γ^+ T cells rather than $CD4^+$IFN-γ^+ T cells. These results all indicated that CD137 agonists could promote the early activation, memory, and effector function of splenic T cells, and mild photothermal therapy rarely affected their activities.

As the key antigen-presenting cells, mature DCs are indispensable to the initiation of the adaptive immune response. However, this progress is often impeded by MDSCs. We thus explored whether TURN could promote DC maturation and decrease MDSCS abundance *in vitro* (Fig. 3E). DC maturation was detected in several groups: I) free medium; II) Gel only (Gel); III) PL-loaded gel without laser irradiation (GP); IV) PL-loaded gel with laser irradiation (GP + L); V) CD137 agonists, RGX-104 and PL-coloaded gel without laser irradiation (GPCR); or VI) CD137 agonists, RGX-104 and PL-coloaded gel with laser irradiation (TURN-TURN). Among them, free medium, Gel, and GP displayed similar mature DCs ratios while GP + L was higher, which might be caused by mild PTT-prompted tumor antigens release (Fig. 3F). Moreover, TURN showed more mature DCs than the others, which meant TURN did promote effective DCs maturation *in vitro* (Fig. 3G). In addition, the

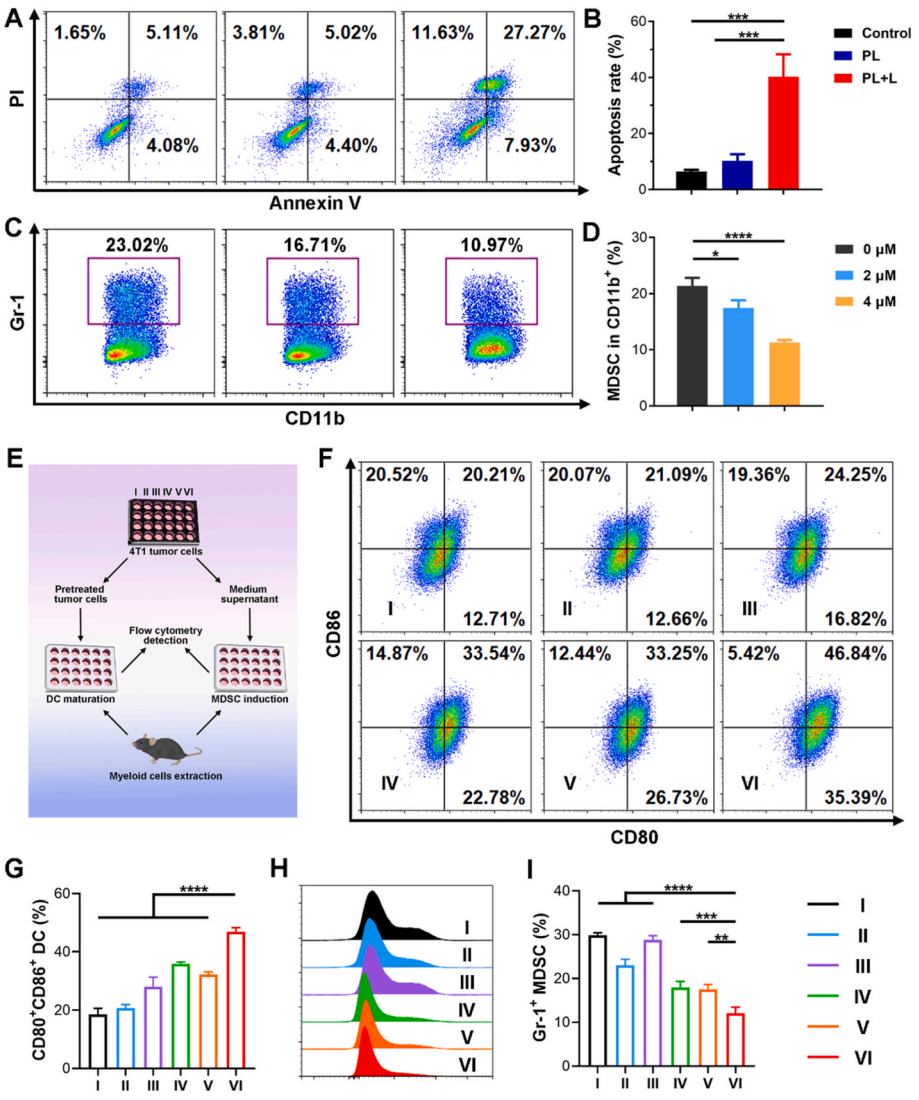

Fig. 3. TURN promoted DCs maturation and inhibited MDSCs abundance. A) Representative flow cytometry charts and B) statistical analysis of apoptosis cells in different groups. C) The flow cytometric analysis of MDSCs after incubation with RGX-104 at different concentrations and their D) statistical analysis. E) Scheme illustration of DC maturation and MDSC induction *in vitro*. F) Flow cytometry plots and G) statistical analysis of mature DCs with different treatments. The groups were I) free medium, II) Gel, III) GP, IV) GP + L, V) GPCR, and VI) TURN. H) MDSCs abundance detected by flow cytometry and I) its quantitative analysis. (Data are presented as mean ± SD, $*p < 0.05$, $**p < 0.01$, $***p < 0.001$, $****p < 0.0001$).

abundance of MDSCs within TME is related to the immune "escape" phase. Herein, we verified TURN could reduce MDSCs abundance *in vitro*. Compared with the free medium, the ratio of MDSCs was decreased in GP + L, GPCR, and TURN (Fig. 3H and I), which meant both PTT and RGX-104 could reduce the proportion of MDSCs. Furthermore, TURN displayed the lowest MDSCs ratio (TURN *vs* NS: 12.05 ± 1.14 *vs* 29.88 ± 0.44, $p < 0.0001$), which supported TURN could gain control over MDSC.

2.3. TURN inhibited local tumor progress in vivo relying on cancer immunoediting phases regression

Extrinsic inevitable immunosuppression and intrinsic immunogenicity scarcity within triple-negative breast cancer often led to it being a "cold" tumor with severe immune escape and terrible tumor progression. We thus established 4T1 tumor-bearing mice to determine whether TURN could reverse cancer immunoediting phases from "escape" to "equilibrium", and even "elimination". Specifically, 4T1 tumor-bearing mice received different *in situ* treatment options as follows: I) Normal saline (NS); II) Gel; III) GP; IV) GP + L; V) GPCR; or VI) TURN (Fig. 4A). Tumor volume and body weights (Fig. S13) of mice receiving several treatment options were monitored and recorded. As shown in Fig. 4B, NS, Gel, GP, and GP + L could not inhibit 4T1 tumor progress, while GPCR and TURN inhibited tumor growth significantly. Compared with GPCR (66.90 %), TURN (91.73 %) displayed a higher tumor inhibition rate. It might be due to the release of tumor antigens or remodeling of the tumor immune microenvironment rather than direct tumor ablation. Individual tumor volume curves (Fig. S14) and maximal change of tumor volume (Fig. 4C) also supported that TURN could inhibit tumor progress significantly. In line with tumor volume, median survival was also observed and there was no significance among NS, Gel, GP, and GP + L. Nonetheless, GPCR and TURN prolonged median survival significantly. The survival rate of TURN was still kept at 16.67 % after 60 days post-tumor inoculation (Fig. 4D). In addition, H&E staining (Fig. S15) and serum biochemistry analysis (Fig. S16) of different groups showed TURN had no obvious systemic toxicity. Hemolysis assay also exhibited that the hydrogel scaffold would not cause hemolysis (Fig. S17). In summary, TURN could gain control over tumor regression effectively.

To explore the antitumor mechanism of TURN, we analyzed the immune landscape of tumors with different treatments (Fig. 4E). Given

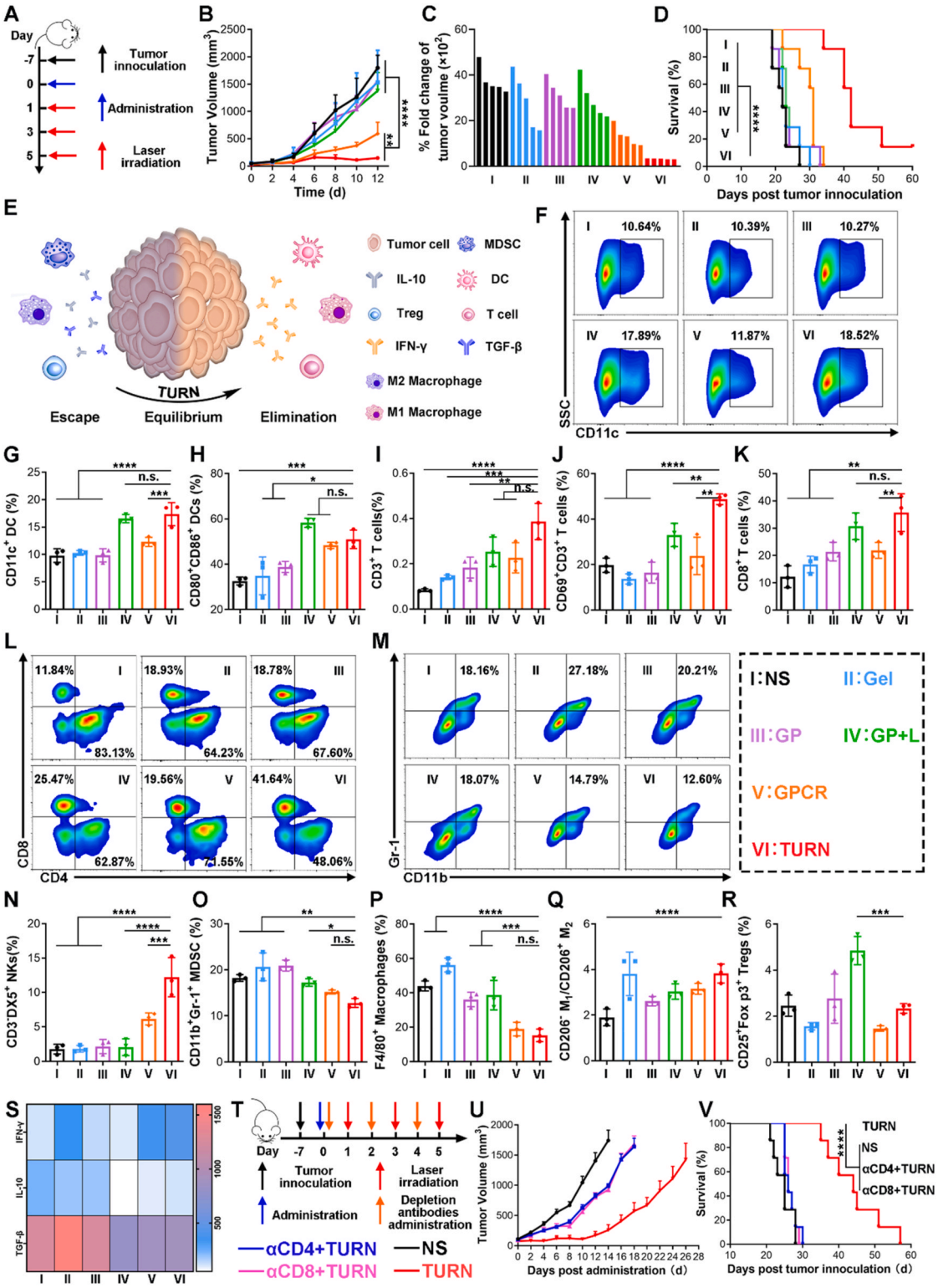

Fig. 4. TURN inhibited local tumor progress and reversed cancer immunoediting phases. A) Scheme illustration of the subcutaneous 4T1 tumor models (n = 5). Mice were treated with I) NS, II) Gel, III) GP, IV) GP + L, V) GPCR, and VI) TURN. B) Tumor volume curves of different groups. C) Maximal fold changes of tumor volume before and after administration. D) Survival curves of tumor-bearing mice after different treatments. E) Scheme illustration of TURN-induced cancer immunoediting phases regression (n = 3). F) Flow cytometry charts and G) statistical analysis of DCs within TME. H) DCs maturation within TME. I) Infiltration and J) activation of $CD3^+$ T cells in TME. K) The percentage and L) The flow cytometric plots of $CD8^+$ T cells gated on $CD3^+$ T cells. M) MDSCs detected by flow cytometry. Quantitative analysis of N) NK cells, O) MDSCs, and P) TAMs in tumor. Q) The ratio of M1 to M2. R) Quantitative analysis of Tregs in TME. S) Tumoral cytokines (IFN-γ, IL-10, and TGF-β) heatmap. T) Scheme illustration of T cells depleted, subcutaneous 4T1 tumor model (n = 5). U) The tumor volume and V) survival curves of mice with different treatments. (Data are presented as mean ± SD, $*p < 0.05$, $**p < 0.01$, $***p < 0.001$, $****p < 0.0001$).

immunogenicity improvement would affect DC-T cell interaction-dependent adaptive immune responses, we hypothesized that DC-T cell crosstalk was crucial for TURN-reversed cancer immunoediting phases. The infiltration of DCs in GP + L (16.53 % ± 0.62 %) and TURN (17.63 % ± 1.72 %) exceeded that of NS (9.79 % ± 1.01 %) significantly, which might be related to laser irradiation-triggered tumor antigens exposure (Fig. 4F and G). In addition, DC maturation in TME showed similar trends with DC infiltration (Fig. 4H and Fig. S18). Moreover, tumor-infiltrating T cells were also observed. GP + L, GPCR, and TURN displayed an elevated ratio of T cells compared with the others (Fig. 4I). Matching the above analysis, $CD69^+$ activated T cells were also related to laser irradiation because both GP+L and TURN owned more activated T cells than the other (Fig. 4J and Fig. S19). As shown in Fig. 4K and L, $CD8^+$ T cells in TURN were almost twice more than NS (TURN *vs* NS: 35.73 % ± 5.66 % *vs* 12.23 % ± 3.26 %, $p < 0.0001$). In addition, TURN also improved tumor-infiltrating NK cells (Fig. 4N and Fig. S20).

Typical tumor-infiltrating immunosuppressive cells, for example, MDSCs, M2 macrophages, and regulatory T cells (Tregs) were all monitored to explore whether TURN could unshackle extrinsic inevitable immunosuppression. The change of MDSCs *in vivo* (Fig. 4M and O) was similar to what had been depicted *in vitro* (Fig. 3H and I). Gel (20.64 % ± 2.47 %) and GP (20.91 % ± 0.97 %) showed an increased ratio of MDSCs compared with NS (18.21 % ± 0.59 %). On the contrary, GP + L (17.23 % ± 0.67 %) showed a reduced MDSCs ratio than GP, which meant mild PTT could downregulate MDSCs to a certain extent. Additionally, GPCR (15.18 % ± 0.35 %) and TURN (12.77 % ± 0.78 %) further reduced the MDSCs ratio due to RGX-104. TURN integrated the function of RGX-104 and mild PTT and displayed the lowest MDSCs proportion, which indicated TURN could decrease MDSCs abundance within TME significantly. The other two immunoinhibitory cells, TAM and Tregs, were also analyzed in our study. Among them, TAM decreased sharply only in GPCR and TURN (Fig. 4P and Fig. S21). The ratio of M1 and M2 macrophages (Fig. 4Q and Fig. S22) in TAM was calculated. TURN showed an elevated M1/M2 ratio than the others, which could be explained by immunogenicity improvement-induced M1 increase and immunosuppression relief-induced M2 decrease. GP + L and TURN improved the ratio of Tregs compared with GP and GPCR, respectively. However, TURN showed fewer Tregs than GP + L supporting that TURN could change Tregs abundance to a certain extent (Fig. 4R and S23).

Tumoral cytokines were another evaluation indicator of the immune state within TME, we thus monitored tumoral IL-10, TGF-β1, and IFN-γ (Fig. 4S). TURN reduced IL-10 and TGF-β1 supporting that TURN could reverse immunosuppression successfully. Furthermore, TURN caused the highest tumoral IFN-γ concentration supporting that TURN could improve immunogenicity and reverse the cancer immunoediting phases.

T cells were the main force against tumor progress. Hence, we utilized depletion antibodies against $CD4^+$ T cells or $CD8^+$ T cells to explore the key executor of TURN against tumor growth. The scheme of administration was shown in Fig. 4T. Tumor volume and survival rates (Fig. 4U and V) demonstrated that both $CD4^+$ and $CD8^+$ T cells, in TURN, would be participating in antitumor effects in primary tumors. They together form the defense against tumor progress.

2.4. TURN levered a potent systemic immune response in vivo

Considering the excellent local antitumor efficiency of TURN, we hypothesized TURN could also lever a systemic immune response (Fig. 5A). Therefore, T cells and conventional type 1 dendritic cell (cDC1) in lymph nodes were detected (Fig. 5B). The classic antigen cross-presentation cells: $CD103^+$, $CD8\alpha^+$ cDC1, and $CD103^+CD8\alpha^+$ cDC1 did raise in TURN (Fig. 5C), which indicated that TURN might lever a systemic immune response. We thus explored T cells in lymph nodes. Both $CD8^+$ and $CD4^+$ T cells (Fig. 5D and Fig. S24) exhibited obvious elevation in TURN, which meant TURN could lever a potent systemic immune response although with peritumoral administration.

Furthermore, the splenic immune cells were also analyzed. TURN led to the change of T cells, MDSCs, and NK cells in the spleen. $CD4^+$ T cells of TURN were 1.40 times than those of NS (Fig. 5E). The proportion of $CD8^+$ T cells (Fig. 5F) was increased in GPCR (15.25 % ± 0.68 %) and TURN (21.26 % ± 0.42 %) when compared with NS (8.65 % ± 0.72 %), which meant TURN could promote the proliferation of T cells in the spleen although with peritumoral administration. TURN could not only upregulate the proportion of T cells (Fig. 5G) in the spleen but also promote their functions. $CD69^+$, IFN-γ^+, and Granzyme B^+CD4^+ T cells were determined among all groups. The proportion of $CD69^+$ (Fig. 5H and Fig. S25), IFN-γ^+ (Fig. S26), and Granzyme B^+ (Fig. 5I and Fig. S27) $CD4^+$ T cells in TURN was 1.87, 7.51, and 5.29-fold higher than those of NS respectively. In addition, the ratio of $CD69^+CD8^+$ T cells (Fig. 5J and Fig. S28) in GPCR and TURN was similar and more than in NS. Moreover, IFN-γ^+ (Fig. 5K and Fig. S29) and Granzyme B^+CD8^+ T cells (Fig. 5K and Fig. S30) in TURN were also more than those of NS (3.91-fold and 14.79-fold, respectively). Finally, splenic MDSCs (Fig. 5L and M) were decreased in GP + L, GPCR, and TURN. MDSCs reduced extensively in TURN, which was consistent with tumoral MDSC. TURN could also increase $CD3^-DX5^+$ NK cells in the spleen (Fig. 5N and Fig. S31).

In addition, Pro-inflammatory cytokines IL-6 and IFN-γ (Fig. 5O) in serum also supported that TURN could induce a potent systemic immune response *in vivo*.

4T1 surgical resection models were then performed to detect whether TURN could launch a long-term immune response. A scheme illustration was displayed in Fig. 5P. Two weeks post-surgery, spleens of mice were obtained to detect the proportion of central memory T cells (T_{CM}) and effector memory T cells (T_{EM}). As shown in Fig. 5Q, T_{CM} (Fig. S32) gated in $CD8^+$ T cells was increased significantly in TURN when compared with NS (TURN *vs* NS: 61.08 % ± 0.92 % *vs* 32.95 % ± 3.33 %, $p < 0.01$), which demonstrated that TURN could improve the immune memory effect. In addition, TURN also improved the proportion of T_{CM} gated in $CD3^+$ T cells (Fig. 5R and S33) rather than T_{EM}. These results meant TURN might be an effective strategy to launch long-term immune memory.

2.5. TURN in the primary tumor triggered regression of the secondary tumor

TURN could induce a potent systemic immune response with peritumoral administration. Therefore, we established bilateral 4T1 tumor models to verify whether TURN could inhibit secondary tumor growth. The scheme illustration was shown in Fig. 6A. Tumor volume curves of primary, and secondary tumors and the body weights of mice were depicted in Fig. 6B, C, and 6D, respectively. TURN showed obvious tumor growth inhibition both in primary and secondary tumors while the others could not. In detail, TURN induced a 92.23 % tumor inhibition rate in the primary tumor and an 83.38 % tumor inhibition rate in the secondary tumor when compared with NS. Moreover, images (Fig. S34) and weights of primary (Fig. 6E) and secondary tumors (Fig. 6F) also supported that TURN could not only eliminate local tumor lesions but also induce potent systemic immune responses, thus inhibiting secondary tumor growth significantly. The individual tumor volume curves of secondary tumors were displayed in Fig. 6G. To explore the main force against secondary tumor growth, T-cell infiltration of secondary tumors was analyzed (Fig. 6H). Interestingly, $CD4^+$ T cells in the secondary tumor had almost no difference among all groups (Fig. 6I), while $CD8^+$ T cells raised significantly in the TURN group (Fig. 6J and K). Compared with NS (3.77 % ± 1.35 %), TURN (23.23 % ± 1.05 %) increased 6.17 times the proportion of $CD8^+$ T cells.

Subsequently, depletion antibodies against $CD4^+$ T cells or $CD8^+$ T cells were used to further evaluate the major factors of TURN against the secondary tumor growth (Fig. 6L). Different from primary tumors (Fig. 4U), $CD8^+$ T cell blockade led to the failure of TURN to inhibit the

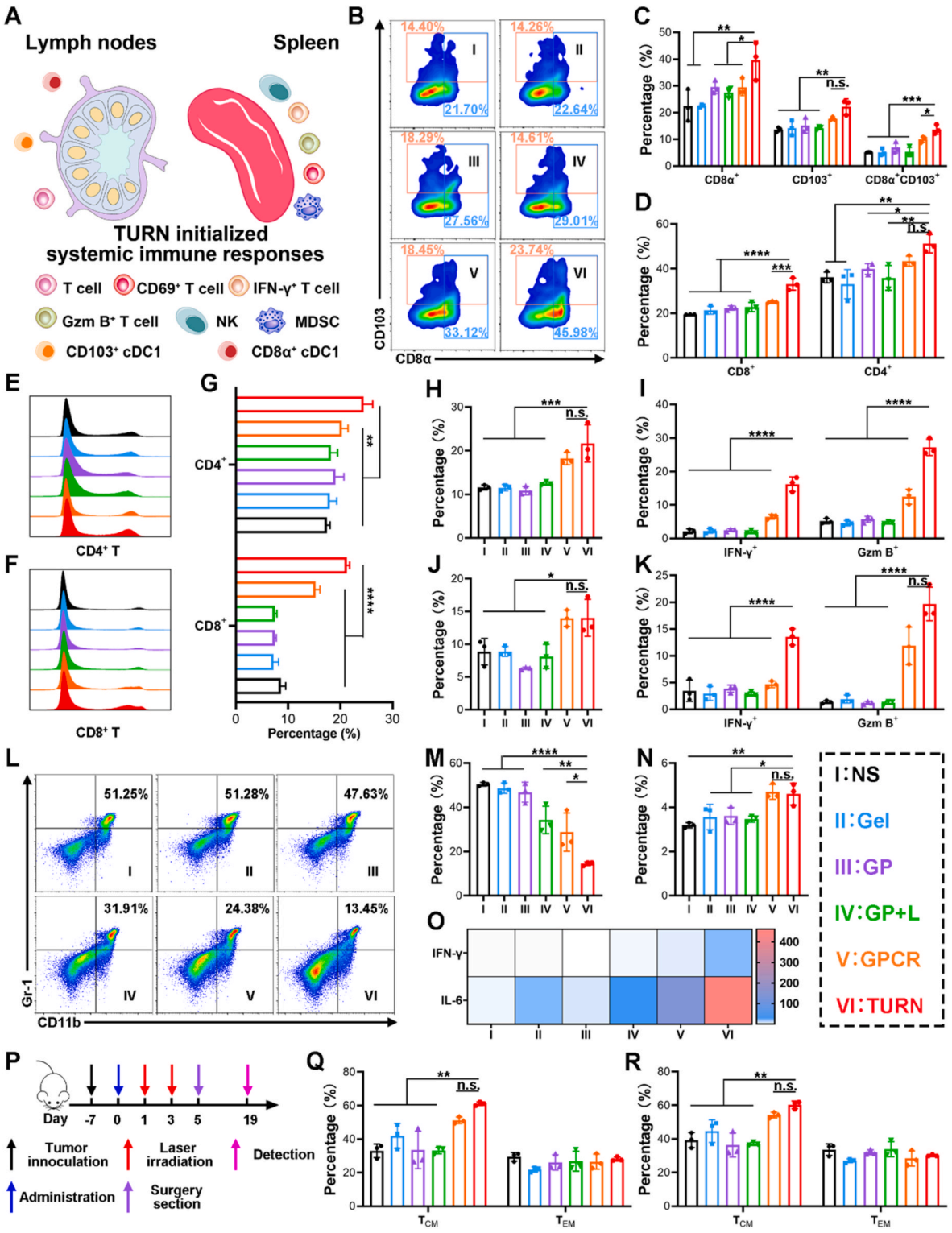

Fig. 5. TURN levered a potent systemic immune response *in vivo*. A) Scheme illustration of TURN levered a systemic immune response (n = 5). Mice were treated with I) NS, II) Gel, III) GP, IV) GP + L, V) GPCR, and VI) TURN. Some immune cells in lymph nodes were shown from B) to D). B) Flow cytometry charts and C) statistical analysis of cDC1. D) Quantitative analysis of T cells. Some immune cells in spleen were shown from E) to N). Flow cytometric plots of E) $CD4^+$ and F) $CD8^+$ T cells. G) Quantitative analysis of T cells in the spleen. H) $CD69^+CD4^+$ T cells. I) IFN-γ^+ and Granzyme B^+CD4^+ T cells. J) $CD69^+CD8^+$ T cells. K) IFN-γ^+ and Granzyme B^+CD8^+ T cells. L) Representative flow cytometry charts and M) statistical analysis of MDSCs. N) Quantitative analysis of NK cells. O) The heatmap of cytokines (IFN-γ, IL-6) in serum. P) Scheme illustration of TURN launched a long-term immune memory (n = 3). T_{CM} and T_{EM} gated on Q) $CD8^+$ T cells and R) $CD3^+$ T cells in the spleen. (Data are presented as mean ± SD, $^*p < 0.05$, $^{**}p < 0.01$, $^{***}p < 0.001$, $^{****}p < 0.0001$).

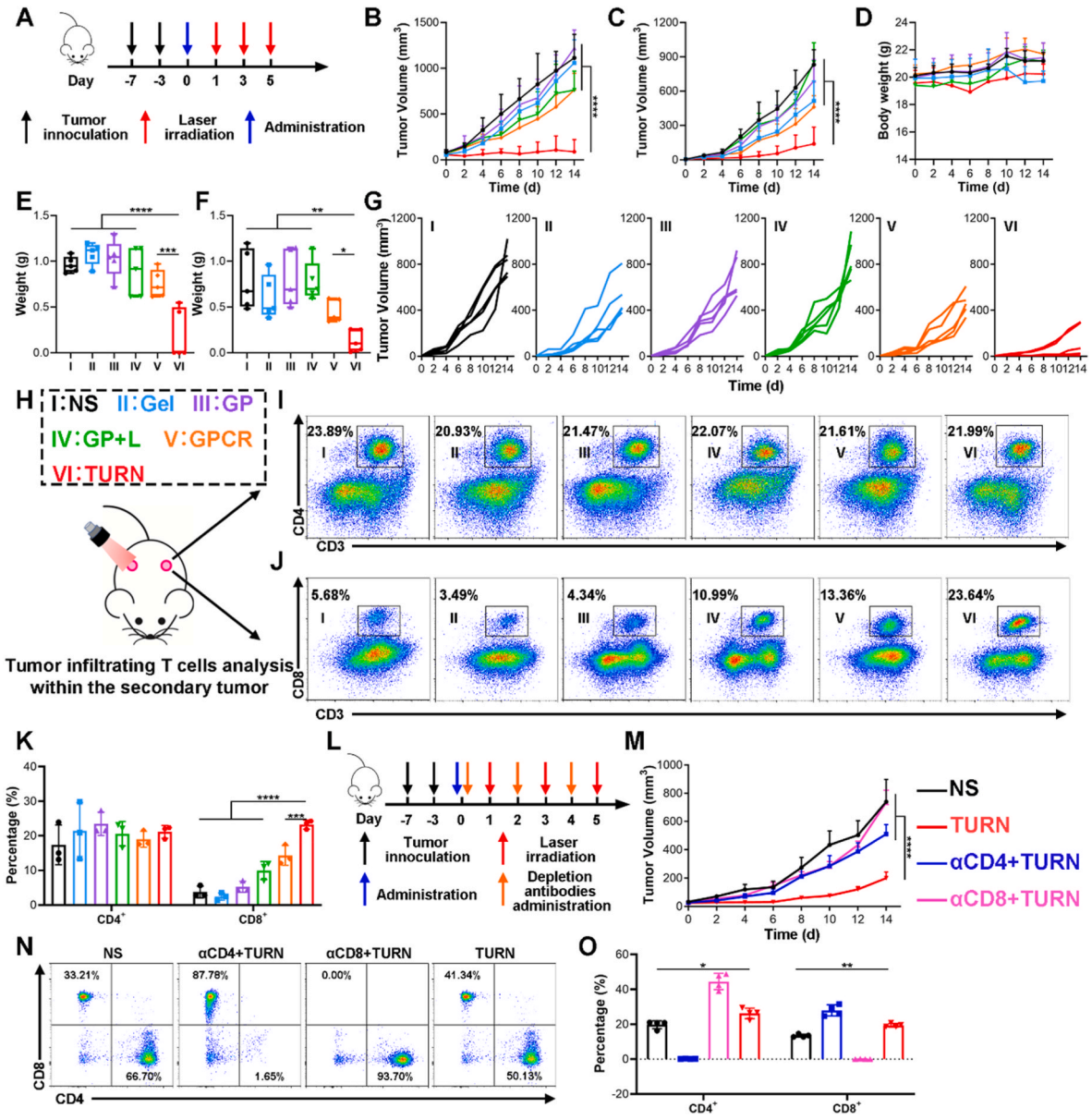

Fig. 6. TURN in the primary tumor triggered regression of the secondary tumor. A) Scheme illustration of the subcutaneous 4T1 bilateral tumor models. Mice were treated with I) NS, II) Gel, III) GP, IV) GP + L, V) GPCR, and VI) TURN (n = 5). Tumor volume curves of B) primary tumors and C) Secondary tumors. D) Body weights of mice received different treatments. Tumor weights of E) primary tumors and F) Secondary tumors. G) Individual tumor volume curves of secondary tumors in different groups. H) Scheme illustration of tumor-infiltrating T cells analysis within the secondary tumor. Representative flow cytometry charts of I) $CD4^+$ and J) $CD8^+$ T cells in TME of the secondary tumor. K) Statistical analysis of tumor-infiltrating T cells within the secondary tumor. L) Scheme illustration of the establishment of T cells depleted, bilateral 4T1 tumor models (n = 5). Mice were treated by NS, TURN, αCD4+TURN, and αCD8+TURN. M) Tumor volume curves of the secondary tumor in different groups. N) Flow cytometric plots of $CD4^+$ and $CD8^+$ T cells gated on $CD3^+$ T cells. O) Quantitative analysis of splenic T cells gated on lymphocytes with different treatments. (Data are presented as mean ± SD, $*p < 0.05$, $**p < 0.01$, $***p < 0.001$, $****p < 0.0001$).

secondary tumor (Fig. 6M), which revealed that $CD8^+$ T cells might be mainly involved in anti-secondary tumor immune response. Moreover, we analyzed splenic $CD4^+$ and $CD8^+$ T cells in $CD3^+$ T cells (Fig. 6N). It was obvious that the proportion of $CD4^+$ or $CD8^+$ T cells in TURN was more than that of NS. To evaluate whether $CD4^+$ and $CD8^+$ T cells were improved with TURN treatment, we analyzed the proportion of $CD4^+$ and $CD8^+$ T cells in lymphocytes (Fig. 6O). The results demonstrated TURN could promote the proliferation of both $CD4^+$ and $CD8^+$ T cells in the spleen again.

2.6. TURN was a broad-spectrum ISV tactic

CT26 subcutaneous tumor model was established to explore whether TURN was a broad-spectrum vaccine tactic for tumor treatment. The scheme illustration was shown in Fig. 7A. Tumor volume and body weights of CT26 tumor-bearing mice were both depicted during treatments (Fig. 7B and C). TURN triggered tumor regression compared with NS (tumor inhibition rate: 95.95 %). The body weights of mice displayed no differences among all groups. Tumor weights corroborated the above tumor volume curves (Fig. 7D). GPCR showed reduced tumor weight while TURN showed the lightest tumor weights. The individual tumor volume curves were also in Fig. 7E. Moreover, it was also verified whether TURN could induce a systemic immune response in bilateral CT26 tumor models (Fig. 7F). In comparison with NS, the tumor volume of primary (Fig. 7G) and secondary tumors (Fig. 7H) in TURN exhibited similar tumor inhibition rates, 97.45 %, and 97.57 % respectively.

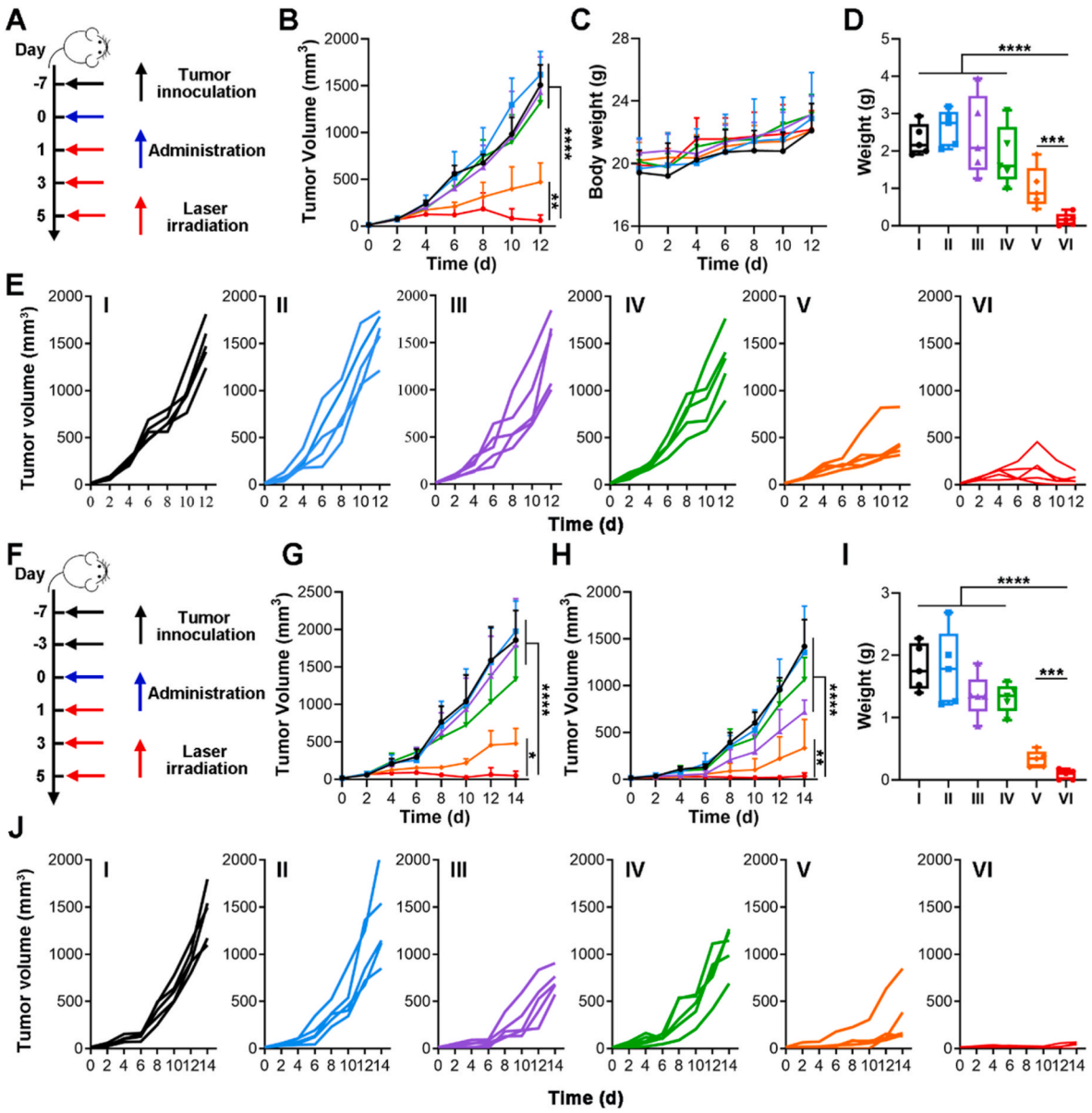

Fig. 7. TURN exhibited the local and systemic anti-tumor effect in CT26 tumor models. A) Scheme illustration of the subcutaneous CT26 tumor models (n = 5). Mice were treated with I) NS, II) Gel, III) GP, IV) GP + L, V) GPCR, and VI) TURN. B) Tumor volume curves of different groups. C) Body weights and D) tumor weights of mice received different treatments. E) Individual tumor volume curves of different groups. F) Scheme illustration of the subcutaneous CT26 bilateral tumor models (n = 5). Mice were treated with I) NS, II) Gel, III) GP, IV) GP + L, V) GPCR, and VI) TURN. Tumor volume curves of G) primary tumors and H) secondary tumors with different treatments. I) Tumor weights and J) Individual tumor volume curves of the secondary tumors. (Data are presented as mean ± SD, $*p < 0.05$, $**p < 0.01$, $***p < 0.001$, $****p < 0.0001$).

Consistent with the aforesaid tumor volume of secondary tumors, TURN also led to a statistical reduction of the secondary tumor weights in Fig. 7I (TURN *vs* NS: 1.81 ± 0.34g *vs* 0.08 ± 0.07g, $p < 0.0001$). In addition, the individual tumor volume curves of the secondary tumor were also depicted in Fig. 7J. The body weights of mice with different treatments revealed diverse results, NS, Gel, GP, and GP + L showed heavier body weights than GPCR and TURN (Fig. S35), which could be explained by their heavier bilateral tumor weights. Overall, we verified that TURN might be universal for tumor treatments and could induce systemic immune response even with local peritumoral administration.

3. Conclusion

Cancer immunoediting was proven to occur in immune-proficient mice and humans naturally [47,48]. It would proceed through three phases, “elimination”, “equilibrium” and “escape”. The “elimination” phase often occurrs in the early tumor, when innate immune cells, adaptive immune cells, and their effector molecules inhibit tumorigenesis jointly [49]. However, due to the heterogeneity and genetic instability of tumor cells, “equilibrium” happened and would be cumulative over extended periods. In detail, those cells that survived under the pressure of immune selection would evolve new clones with reduced immunogenicity, which constituted the main force resistant to immune attack [50,51]. The variants clone of “equilibrium” grew wildly and became visible even with intact immunity, which marked the advent of “escape” [52–54]. In this stage, terrible proliferation and survival abilities of tumors, poor antigen exposure, and complex immunosuppression co-build fortifications against antitumor immune responses.

ISV represents a promising vaccine strategy to break the pro-tumor barrier of the “escape” phase owing to complete tumoral antigen

exposure. However, ISV is subjected to inevitable extrinsic immunosuppression and intrinsic immunogenicity scarcity. To remove the shackle of immunosuppression and amplify the abundance of tumoral antigens, we employed a tumor-activated and optically reinforced immunoscaffold for cancer immunoediting phases regression. TURN could induce DC maturation and MDSCs abundance decline significantly *in vitro*. Subsequently, we verified that TURN could inhibit over 90 % of tumor progress in contrast to the NS group in 4T1 tumor models *in vivo*. The tumoral immune landscapes analysis exhibited that TURN could lead to the remodeling of the tumor immune microenvironment, thus reversing the local cancer immunoediting phases. In detail, masses of immunosuppressive cells (MDSCs, M2, and Tregs) were reduced and replaced by an influx of anti-tumor immune cells (DCs, M1, and T cells). Moreover, we investigated that TURN could lever a potent systemic antitumor immune response and launch a long-term immune memory against the tumor, thus inhibiting secondary tumor growth. Overall, TURN was an effective ISV strategy that could trigger local cancer immunoediting phases regression and pry back systemic antitumor immune responses, thus inhibiting local tumor progression and preventing secondary tumor growth.

Furthermore, we explored the effectiveness of TURN on CT26 tumor-bearing mice. The excellent tumor inhibition ability of TURN in primary and secondary CT26 tumors supported that TURN might be a broad-spectrum vaccine tactic with the prospect. However, the concrete tumoral immune landscape of CT26 treated by TURN was still unclear, although TURN exhibited better efficacy for CT26 than 4T1. Additionally, exploring broad-spectrum ISV strategies to reverse the cancer immunoediting phases effectively is still in its infancy, more attention should be paid to it. In summary, TURN is a potent ISV strategy and provides a novel sight from the immunoediting phases' perspective.

4. Materials and methods

4.1. Materials

Stearic acid, lauric acid, soybean lecithin, sodium hyaluronate, *N*-hydroxysuccinimide (NHS), sodium periodate ($NaIO_4$), and 1-Ethyl-3-(3-dimethylaminopropyl)carbodiimide hydrochloride (EDCI) were purchased from Sigma-Aldrich (America). DSPE-mPEG$_{2000}$ was obtained from Advanced Vehicle Technology Pharmaceutical Tech Co., Ltd (Shanghai, China). RGX-104 was provided by RayStarBio (Hangzhou, China). Methyl 3-mercapto propionate, dopamine hydrochloride, gamma polyglutamic acid (PGA), β-mercaptoethanol and 2-(*N*-Morpholino)ethanesulfonic acid (MES) were purchased from Macklin (Shanghai, China). Recombinant mouse GM-CSF and IL-4 were obtained from Peprotech (Rocky Hill, NJ, USA). Fetal Bovine Serum was purchased from ExCell Bio (cat: FSP500; Shanghai, China) and Haixing Bioscience (cat: FBP-C520; Suzhou, China). Mouse IL-6, TGF-β, and IL-10 ELISA kits were acquired from Biolegend (America), and mouse IFN-γ ELISA kits were acquired from Invitrogen (America). Anti-CD3-PE-Cy7, anti-CD4-FTIC, anti-CD4-APC, anti-CD8α-APC, anti-CD8α-FITC, anti-CD69-PE, *anti*–IFN–γ-PE, *anti*-Granzyme B-Pacific Blue, anti-CD44-FITC, anti-CD62L-APC, anti-DX5-PE, anti-CD11c-FITC, anti-CD11c-PE, anti-CD103-APC, anti-CD11b-PE, anti-CD11b-FITC, *anti*-F4/80-PE, anti-CD80-APC, anti-CD86-PE-Cy7, anti-CD206-APC, *anti*-Gr-1-PE, anti-CD25-FITC, *anti*-Foxp3-APC, anti-CD45-APC were purchased from Biolegend (America).

4.2. Cells and animals

4T1 and CT26 cells were obtained from the American Type Culture Collection (ATCC; Manassas, VA, USA). Female BALB/c and C57BL6 mice (6–8 weeks) were provided by HUAFUKANG BIOSCIENCE (Beijing, China). All animal experiments were conducted according to the experimental guidelines of the Animal Experimental Ethics Committee of Sichuan University.

4.3. Preparation, purification, and characterization analysis of PDA and PL

PDA nanoparticles were prepared by auto polymerization of dopamine. Dopamine was added into an alkalescent Ethanol-Water Solution dropwise and auto-polymerized for 48 h at 30 °C. The mixture was centrifuged at 15,000 rpm for 30 min. The sediment was collected and washed twice, subsequently. The thin film hydration-ultrasonic method was used for the preparation of PL nanoparticles. In brief, stearic acid, lauric acid, soybean lecithin, and DSPE-mPEG$_{2000}$ were dissolved in chloroform respectively, which were then mixed for rotatory evaporation at 55 °C. PDA aqueous solution was added into the flask subsequently and hydrated for 30 min. After ultrasonicated for 6 min, the acquired solution was then dipped into ice water for 5 min. The hydrodynamic diameters of PDA and PL were measured with a Malvern spray analyzer and their morphology was observed under a transmission electron microscope. Ultraviolet and visible spectrophotometers and Fourier infrared spectrometers were used to detect their absorption of UV and functional group structure, respectively.

4.4. Synthesis, preparation, and characterization analysis of hydrogel and PL-loaded hydrogel

Sodium hyaluronate was oxidized by $NaIO_4$ for 12 h and acquired after dialysis and lyophilization as matrix A (OHA). By adding concentrated sulfuric acid dropwise into the mixture of methyl 3-mercapto propionate, acetone, and anhydrous sodium sulfate, the raw product was synthesized at 70 °C for 10 h with condensation reflux. S-ADH was acquired after separation and purification by column chromatogram. Subsequently, S-ADH reacted with hydrazine hydrate at a ratio of 1:6 in methyl alcohol overnight to get S-ADH-NH_2. Then, S-ADH-NH_2 was mixed with PGA and catalyzed by EDCI and NHS to synthesize PGA-S-ADH in MES buffer at pH 5.5. Finally, PGA-S-ADH was got after dialysis and lyophilization as matrix B. The hydrogel was formed by mixing O-HA with PGA-S-ADH at a final concentration of 10 mg/mL, respectively. The PL-loaded hydrogel was prepared by mixing PL concentrate into matrix B, and then into matrix A.

4.5. The photothermal conversion performance of PDA and PL NPS

The change of temperature of PDA and PL NPS at different concentrations was measured during exposure to a near-infrared laser (808 nm) at different power densities (1.0, 2.0 W cm^{-2}) for 10 min. To verify the thermal stability of PDA and PL NPS, the temperature was recorded while they were irradiated by laser at 2.0 W cm^{-2} for 10 min and cooled naturally to 30 °C. The on-off cycle was repeated five times.

4.6. Degradation of PDA and PL NPS when treated with hydrogen peroxide

PDA and PL NPS at the same concentration (100 μg/mL) were treated with 1 mM hydrogen peroxide to observe their behaviors. To detect the degradation, the photothermal conversion efficiency of PDA and PL NPS was measured. Briefly, PDA and PL NPS at the same concentration (100 μg/mL) were dialyzed in 10 mM hydrogen peroxide within a dialysis tube (Molecular weight cut-off: 3500 kDa). They were collected at 0 h, 6 h, 12 h, 24 h, 36 h, and 48 h. Subsequently, we measured their photothermal conversion performance. Photothermal conversion efficiency change induced by the degradation of PDA or PL was calculated by the following formula:

$$\frac{\Delta T_X}{\Delta T_0}(\%) = \frac{T_X^{'} - T_X}{T_0^{'} - T_0} \times 100\%$$

In the formula, ΔT_x means the change of temperature at 6 h, 12 h, 24 h, 36 h, or 48 h after irradiation for 10 min, and ΔT_0 means the change of

temperature at 0 h after exposure to laser for 10 min.

4.7. Detection of photothermal effect in vivo

A subcutaneous murine breast tumor model was established to evaluate the photothermal effect of PL-loaded hydrogel. In brief, wild BALB/c female mice received a subcutaneous injection of 4T1 tumor cells (1×10^6 cells/mouse) on the right flank back. Upon tumor volume being up to 100 mm^3, mice would be divided into three groups evenly as follows: NS, Gel + PDA, and Gel + PL. All three groups received laser irradiation for 10 min at 2 W/cm^2 at specific moments after administration, during which the temperature of the tumor had been measured in real-time.

4.8. In vitro effect of PDA, PL

Cytotoxicity of PDA and PL with or without laser irradiation was evaluated by MTT assay. Specifically, 4T1 cells were seeded into 96-well plates and cultured for 24 h. Then, PDA or PL NPS at different concentrations were diluted into a medium and co-cultured with 4T1 cells for another 24 h in laser-free groups. For the cytotoxicity of PDA and PL NPS with laser, 4T1 cells were incubated with PDA and PL for 6 h and received laser irradiation (2.0 W cm^{-2}, 10 min). After 24 h, the 4T1 cells were co-cultured with MTT (20 μL, 5 mg/mL) for 4 h at 37 °C and measured at 570 nm. To detect the apoptosis of PL NPS with or without laser irradiation, 4T1 cells were collected and analyzed by flow cytometry after being marked with FITC-Annexin V and PE-PI.

4.9. In vitro effect of RGX-104

Cytotoxicity of RGX-104 to 4T1 was measured by MTT assay. Briefly, 4T1 cells were seeded into 96-well plates and cultured for 24 h. Subsequently, they were co-cultured with RGX-104 at different concentrations for 24 h and measured at 570 nm. To explore the cytotoxicity of RGX-104 to myeloid-derived suppressor cells, myeloid cells were separated from the tibia and fibula of C57BL6 female mice and cultured in RPMI1640 culture containing GM-CSF (40 ng/mL) for 6 days. On day 3, RGX-104 was co-cultured with myeloid cells. On day 6, myeloid cells were collected, marked with FITC-CD11b and APC-Gr-1, and analyzed with flow cytometry.

4.10. DC maturation detection

Bone marrow-derived cells were separated from the femur and tibia of C57BL6 female mice, which were cultured at 37 °C in RPMI 1640 complete medium containing 20 ng/mL GM-CSF, 10 ng/mL IL-4, 50 μM β-mercaptoethanol and 10 % heat-inactivated FBS for 6 days. On Day 3, the fresh medium was replenished. On Day 6, BMDCs were incubated with PBS, free Gel, GP, GP + L, GPCR, and TURN pretreated 4T1 for 24 h. Subsequently, BMDCs were collected, prepared into single-cell suspensions, and stained by CD11c-PE, CD86-PECy7, and CD80-FITC for flow cytometry.

4.11. MDSC induction

Bone marrow-derived cells were separated from the femur and tibia of C57BL6 female mice, which were cultured at 37 °C in RPMI 1640 complete medium containing 40 ng/mL GM-CSF, 50 μM β-mercaptoethanol, and 10 % heat-inactivated FBS for 6 days. On Day 4, the medium was replenished by the mixture of fresh medium and PBS, free Gel, GP, GP + L, GPCR, and TURN pretreated conditional medium. On Day 6, cells were collected, prepared into single-cell suspensions, and stained by CD11b-FITC, and Gr-1-PE for flow cytometry.

4.12. Anti-tumor assay in vivo

Subcutaneous tumor transplantation models of 4T1 and CT26 were established to evaluate the antitumor efficacy of different groups. BALB/c mice were injected with 4T1 or CT26 tumor cells at 1×10^6 cells/mouse, subcutaneously. They were divided into 6 groups evenly and administered with normal saline, Gel, GP, GP + L, GPCR, and TURN respectively when the tumor volume was about 100 mm^3. The mice that needed laser irradiation were exposed to 1 W/cm^2 near-infrared laser for 10 min at 24, 72, and 120 h post-administration. The tumor volume and the weight of mice were tracked in this process every other day until the tumor volume exceeded 2000 mm^3. Finally, mice were sacrificed and the tumor weights were recorded accurately. For survival observation, the mice whose tumor volume exceeded 2000 mm^3 were regarded as dead.

4.13. Histological analysis

The tumor and main organs (including the heart, lungs, liver, spleen, and kidneys) were collected and fixed in 4 % paraformaldehyde for 5 days. Then, they were processed into the paraffin and cut into slices, and stained with hematoxylin and eosin (H&E).

4.14. Serum biochemistry analysis

Serum was isolated from a blood sample of 4T1-bearing mice after different treatments via eyeball extirpating. ALT, AST, ALB, ALP, TP, UREA, CREA UA, and CKMB were detected to evaluate liver function, renal function, and cardiac function.

4.15. Exploration of the immune response within the tumor microenvironment, lymph nodes, and spleen in 4T1-bearing mice after different treatment

Tumors, lymph nodes, and spleens were obtained from 4T1-bearing mice after different treatments to detect the change in immune cells. Specifically, single-cell suspension of the tumor was gained by cutting and digesting the tumor, which was then stained with anti-CD3-PE-Cy7, anti-CD4-FITC, anti-CD8-APC, anti-CD69-PE, anti-CD11b-FITC, anti-CD206-APC, anti-CD11c-PE, *anti*-Gr-1-APC, anti-CD25-FITC, anti-Fox p3-Alexa Fluor 647. Lymph nodes were punctured into single-cell suspension and stained with anti-CD3-PE-Cy7, anti-CD4-FITC, anti-CD8-APC, anti-CD11c-PE, anti-CD8α-FITC, and anti-CD103-APC. The spleen was ground, filtered, isolated, and then stained with anti-CD3-PE-Cy7, anti-CD4-FITC, anti-CD8-APC, anti-CD69-PE, anti-DX5-APC, anti-CD45-PE, anti-CD11b-FITC, and *anti*-Gr-1-APC. All cells were washed with PBS and analyzed by flow cytometry.

4.16. A bilateral tumor model built for inhibiting secondary tumor growth

BALB/c mice were inoculated with 4T1 or CT26 tumor (1×10^6 cells/mouse) on the right flank back subcutaneously as a primary tumor at Day −7. Tumor-bearing mice were then inoculated with 4T1 or CT26 tumor (5×10^5 cells/mouse) on the left blank back as a distant tumor at Day −3, which would be treated when the primary tumor volume was 100 mm^3. The volume of the primary tumor and abscopal tumor were measured every other day until the primary tumor volume was up to 2000 mm^3. In the end, mice were sacrificed and the weights of primary and abscopal tumors were recorded accurately. The abscopal tumor was collected, cut, and digested into single-cell suspension, which was then washed with PBS and stained with anti-CD3-PE-Cy7, anti-CD4-PE, and anti-CD8-APC. The ratio of tumor-infiltrating T cells was analyzed by flow cytometry.

4.17. Long-term immune-memory effect detected by flow cytometry

BALB/c mice were inoculated with 4T1 (1×10^6 cells/mouse) on the right flank back. They were randomly divided into 6 groups and received different treatments when the tumor volume was 100 mm^3, approximately. Four days post-administration, the tumors were surgically removed. Two weeks later, the mice were sacrificed and the spleens were obtained to determine the ratio of memory T cells. The single-cell suspension was stained with anti-CD3-PE-cy7, anti-CD8-PE, anti-CD44-FITC, and anti-CD62L-APC and analyzed by flow cytometry.

4.18. $CD4^+$ or $CD8^+$ T cells depletion in vivo

4T1 tumor cells were inoculated subcutaneously into BALB/c mice on Day −7. Mice were injected intraperitoneally with anti-CD4 or anti-CD8 on Day 0, 2, and 4, respectively. Moreover, they were peritumorally administrated with GPCR on Day 0, either and exposed to near-infrared laser (2 W/cm^2, 10 min) on Day 1, 3, and 5. The tumor volume was measured and recorded every other day until the tumor volume was up to 2000 mm^3. For survival, mice were taken as dead when the tumor volume exceeded 2000 mm^3. The spleens of those mice were collected, ground, and filtered into single-cell suspension, which was then washed with PBS and stained with anti-CD3-PE-Cy7, anti-CD4-PE, and anti-CD8-APC after lysing red blood cells. Flow cytometry was utilized to analyze T cells in the spleen.

4.19. Enzyme-linked immunosorbent assay

The concentration of IL-6, IFN-γ in serum and IFN-γ, IL-10, and TGF-β in tumor supernatant was detected by ELISA kits according to protocols.

4.20. Statistical and reproducibility

All the data were analyzed with the statistical program, Prism 8.0 GraphPad, and expressed as mean ± standard deviation (SD). The difference between the two groups was analyzed with Student's t-test. One-way ANOVA was used to determine the statistical significance of the difference among three or more three groups. Significant difference was represented as $*p < 0.05$, $**p < 0.01$, $***p < 0.001$, and $****p < 0.0001$.

Ethics approval and consent to participate

All animal experiments were performed under the guidelines approved by the Institutional Animal Care and Treatment Committee of Sichuan University.

CRediT authorship contribution statement

Xinchao Li: Writing – original draft, Software, Methodology, Investigation, Conceptualization. **Xiuqi Liang:** Writing – original draft, Methodology, Investigation, Conceptualization. **Wangxian Fu:** Writing – original draft, Software, Methodology, Investigation. **Rui Luo:** Software, Methodology, Investigation. **Miaomiao Zhang:** Methodology, Investigation. **Xiaorong Kou:** Methodology, Investigation. **Yi Zhang:** Methodology, Investigation. **Yingjie Li:** Investigation. **Dongxue Huang:** Investigation. **Yanjie You:** Methodology. **Qinjie Wu:** Writing – review & editing, Supervision, Funding acquisition, Conceptualization. **Changyang Gong:** Writing – review & editing, Supervision, Funding acquisition, Conceptualization.

Declaration of competing interest

The authors declare that they have no known competing financial interests or personal relationships that could have appeared to influence the work.

Acknowledgments

This work was supported by Funds of Sichuan Province for Distinguished Young Scholar (2021JDJQ0037), the National Natural Science Foundation of China (82372123), Central Guide Local Science and Technology Development Special Project fund (2023FRD05038), and 1·3·5 project for disciplines of excellence, West China Hospital, Sichuan University (ZYYC23004).

Appendix A. Supplementary data

Supplementary data to this article can be found online at https://doi.org/10.1016/j.bioactmat.2024.01.026.

References

[1] C.S. Shemesh, J.C. Hsu, I. Hosseini, B.-Q. Shen, A. Rotte, P. Twomey, S. Girish, B. Wu, Personalized cancer vaccines: clinical landscape, challenges, and opportunities, Mol. Ther. 29 (2021) 555–570.
[2] C. Guo, M.H. Manjili, J.R. Subjeck, D. Sarkar, P.B. Fisher, X.-Y. Wang, Therapeutic cancer vaccines: past, present, and future, Adv. Cancer Res. 119 (2013) 421–475.
[3] E. Blass, P.A. Ott, Advances in the development of personalized neoantigen-based therapeutic cancer vaccines, Nat. Rev. Clin. Oncol. 18 (2021) 215–229.
[4] C.J.M. Melief, T. van Hall, R. Arens, F. Ossendorp, S.H. van der Burg, Therapeutic cancer vaccines, J. Clin. Invest. 125 (2015) 3401–3412.
[5] J. Fucikova, O. Kepp, L. Kasikova, G. Petroni, T. Yamazaki, P. Liu, L. Zhao, R. Spisek, G. Kroemer, L. Galluzzi, Detection of immunogenic cell death and its relevance for cancer therapy, Cell Death Dis. 11 (2020) 1013.
[6] A.D. Garg, P. Agostinis, Cell death and immunity in cancer: from danger signals to mimicry of pathogen defense responses, Immunol. Rev. 280 (2017) 126–148.
[7] G.P. Dunn, A.T. Bruce, H. Ikeda, L.J. Old, R.D. Schreiber, Cancer immunoediting: from immunosurveillance to tumor escape, Nat. Immunol. 3 (2002) 991–998.
[8] M.J. Smyth, G.P. Dunn, R.D. Schreiber, Cancer immunosurveillance and immunoediting: the roles of immunity in suppressing tumor development and shaping tumor immunogenicity, Adv. Immunol. 90 (2006) 1–50.
[9] G.P. Dunn, L.J. Old, R.D. Schreiber, The three Es of cancer immunoediting, Annu. Rev. Immunol. 22 (2004) 329–360.
[10] S.A. Quezada, K.S. Peggs, T.R. Simpson, J.P. Allison, Shifting the equilibrium in cancer immunoediting: from tumor tolerance to eradication, Immunol. Rev. 241 (2011) 104–118.
[11] D. Mittal, M.M. Gubin, R.D. Schreiber, M.J. Smyth, New insights into cancer immunoediting and its three component phases elimination, equilibrium and escape, Curr. Opin. Immunol. 27 (2014) 16–25.
[12] Y. Long, Z. Lu, S. Xu, M. Li, X. Wang, Z. Zhang, Q. He, Self-delivery micellar nanoparticles prevent premetastatic niche formation by interfering with the early recruitment and vascular destruction of granulocytic myeloid-derived suppressor cells, Nano Lett. 20 (2020) 2219–2229.
[13] D. Ding, H. Zhong, R. Liang, T. Lan, X. Zhu, S. Huang, Y. Wang, J. Shao, X. Shuai, B. Wei, Multifunctional nanodrug mediates synergistic photodynamic therapy and MDSCs-targeting immunotherapy of colon cancer, Adv. Sci. 8 (2021) e2100712.
[14] S.R. Wang, Z.Y. Wang, Z.Y. Li, X.G. Zhang, H.T. Zhang, T. Zhang, X.X. Meng, F. G. Sheng, Y.L. Hou, Amelioration of systemic antitumor immune responses in cocktail therapy by immunomodulatory nanozymes, Sci. Adv. 8 (2022) eabn3883.
[15] X.G. Zhang, J.J. Tang, C. Li, Y. Lu, L.L. Cheng, J. Liu, A targeting black phosphorus nanoparticle based immune cells nano-regulator for photodynamic/photothermal and photo-immunotherapy, Bioact. Mater. 6 (2021) 472–489.
[16] C.L. Chen, M.Y. Song, Y.Y. Du, Y. Yu, C.G. Li, Y. Han, F. Yan, Z. Shi, S.H. Feng, Tumor-associated-macrophage-membrane-coated nanoparticles for improved photodynamic immunotherapy, Nano Lett. 21 (2021) 5522–5531.
[17] M.F. Tavazoie, I. Pollack, R. Tanqueco, B.N. Ostendorf, B.S. Reis, F.C. Gonsalves, I. Kurth, C. Andreu-Agullo, M.L. Derbyshire, J. Posada, S. Takeda, K.N. Tafreshian, E. Rowinsky, M. Szarek, R.J. Waltzman, E.A. Mcmillan, C.N. Zhao, M. Mita, A. Mita, B. Chmielowski, M.A. Postow, A. Ribas, D. Mucida, S.F. Tavazoie, LXR/ApoE activation restricts innate immune suppression in cancer, Cell 172 (2018) 825–840.
[18] K. Ni, G. Lan, N. Guo, A. Culbert, T. Luo, T. Wu, R.R. Weichselbaum, W. Lin, Nanoscale metal-organic frameworks for x-ray activated in situ cancer vaccination, Sci. Adv. 6 (2020) eabb5223.
[19] Y. Chao, L.G. Xu, C. Liang, L.Z. Feng, J. Xu, Z.L. Dong, L.L. Tian, X. Yi, K. Yang, Z. Liu, Combined local immunostimulatory radioisotope therapy and systemic immune checkpoint blockade imparts potent antitumour responses, Nat. Biomed. Eng. 2 (2018) 611–621.
[20] T. He, M. Hu, S. Zhu, M. Shen, X. Kou, X. Liang, L. Li, X. Li, M. Zhang, Q. Wu, C. Gong, A tactical nanomissile mobilizing antitumor immunity enables neoadjuvant chemo-immunotherapy to minimize postsurgical tumor metastasis and recurrence, Acta Pharm. Sin. B 13 (2023) 804–818.
[21] S.L. Gong, X.Q. Liang, M.M. Zhang, L. Li, T. He, Y. Yuan, X.C. Li, F.R. Liu, X. Yang, M.L. Shen, Q.J. Wu, C.Y. Gong, Tumor microenvironment-activated hydrogel platform with programmed release property evokes a cascade-amplified immune response against tumor growth, metastasis and recurrence, Small 18 (2022) e2107061.

[22] L. Li, X.Q. Liang, T. He, X.C. Li, X.Z. Huang, N. Wang, M.L. Shen, Y.Q. Shu, R. Wu, M.M. Zhang, Q.J. Wu, C.Y. Gong, Multifunctional light-activatable nanocomplex conducting temperate-heat photothermal therapy to avert excessive inflammation and trigger augmented immunotherapy, Biomaterials 290 (2022) 121815, 290.
[23] A.P. Castano, P. Mroz, M.R. Hamblin, Photodynamic therapy and anti-tumour immunity, Nat. Rev. Cancer 6 (2006) 535–545.
[24] H. Shin, K. Na, Cancer-targetable pH-sensitive zinc-based immunomodulators combined with photodynamic therapy for in situ vaccination, ACS Biomater. Sci. Eng. 6 (6) (2020) 3430–3439.
[25] M. Ahn, T. Lee, K.S. Kim, S. Lee, K. Na, Synergistic approach of antibody-photosensitizer conjugate independent of KRAS-mutation and its downstream blockade pathway in colorectal cancer, Adv. Healthcare Mater. 12 (2023) 2302374.
[26] X. Li, J.F. Lovell, J. Yoon, X. Chen, Clinical development and potential of photothermal and photodynamic therapies for cancer, Nat. Rev. Clin. Oncol. 17 (2020) 657–674.
[27] X. Zhang, J.F. Du, Z. Guo, J. Yu, Q. Gao, W.Y. Yin, S. Zhu, Z.J. Gu, Y.L. Zhao, Efficient near infrared light triggered nitric oxide release nanocomposites for sensitizing mild photothermal therapy, Adv. Sci. 6 (2019) 1801122.
[28] L.P. Huang, Y.N. Li, Y.N. Du, Y.Y. Zhang, X.X. Wang, Y. Ding, X.L. Yang, F.L. Meng, J.S. Tu, L. Luo, C.M. Sun, Mild photothermal therapy potentiates anti-PD-L1 treatment for immunologically cold tumors via an all-in-one and all-in-control strategy, Nat. Commun. 10 (1) (2019) 4871.
[29] Q. Chen, Q.Y. Hu, E. Dukhovlinova, G.J. Chen, S. Ahn, C. Wang, E.A. Ogunnaike, F. S. Ligler, G. Dotti, Z. Gu, Photothermal therapy promotes tumor infiltration and antitumor activity of CAR T cells, Adv. Mater. 31 (2019) e1900192.
[30] X.Y. Ye, X. Liang, Q. Chen, Q.W. Miao, X.L. Chen, X.D. Zhang, L. Mei, Surgical tumor-derived personalized photothermal vaccine formulation for cancer immunotherapy, ACS Nano 13 (2019) 2956–2968.
[31] Z. Wang, Y. Zou, Y.W. Li, Y.Y. Cheng, Metal-containing polydopamine nanomaterials: catalysis, energy, and theranostics, Small 16 (18) (2020) e1907042.
[32] P. Yang, F. Zhu, Z.B. Zhang, Y.Y. Cheng, Z. Wang, Y.W. Li, Stimuli-responsive polydopamine-based smart materials, Chem. Soc. Rev. 50 (14) (2021) 8319–8343.
[33] A.T. Jin, Y.T. Wang, K.L. Lin, L.Y. Jiang, Nanoparticles modified by polydopamine: working as "drug" carriers, Bioact. Mater. 5 (3) (2020) 522–541.
[34] K. Li, H.H. Shi, B.X. Zhang, X.J. Ou, Q.Z. Ma, Y. Chen, P. Shu, D. Li, Y.S. Wang, Myeloid-derived suppressor cells as immunosuppressive regulators and therapeutic targets in cancer, Signal Transduct. Targeted Ther. 6 (1) (2021) 362.
[35] M. Croft, The role of TNF superfamily members in T-cell function and diseases, Nat. Rev. Immunol. 9 (2009) 271–285.
[36] B.K. Choi, D.Y. Lee, D.G. Lee, Y.H. Kim, S.H. Kim, H.S. Oh, C. Han, B.S. Kwon, 4-1BB signaling activates glucose and fatty acid metabolism to enhance CD8(+) T cell proliferation, Cell. Mol. Immunol. 14 (2017) 748–757.
[37] C. Chester, M.F. Sanmamed, J. Wang, I. Melero, Immunotherapy targeting 4-1BB: mechanistic rationale, clinical results, and future strategies, Blood 131 (2018) 49–57.
[38] D.D. Wan, Y.L. Yang, Y.Y. Liu, X.L. Cun, M. Li, S.S. Xu, W. Zhao, Y.Y. Xiang, Y. Qiu, Q.W. Yu, X. Tang, Z.R. Zhang, Q. He, Sequential depletion of myeloid-derived suppressor cells and tumor cells with a dual-pH-sensitive conjugated micelle system for cancer chemoimmunotherapy, J. Contr. Release 317 (2020) 43–56.
[39] C. Chester, S. Ambulkar, H.E. Kohrt, 4-1BB agonism: adding the accelerator to cancer immunotherapy, Cancer Immunol. Immunother. 65 (2016) 1243–1248.
[40] A. Palazon, I. Martinez-Forero, A. Teijeira, A. Morales-Kastresana, C. Alfaro, M. F. Sanmamed, J. Luis Perez-Gracia, I. Penuelas, S. Hervas-Stubbs, A. Rouzaut, M. Ortiz de Landazuri, M. Jure-Kunkel, J. Aragones, I. Melero, The HIF-1 alpha hypoxia response in tumor-infiltrating T lymphocytes induces functional CD137 (4-1BB) for immunotherapy, Cancer Discov. 2 (2012) 608–623.
[41] Y.L. Liu, K.L. Ai, J.H. Liu, M. Deng, Y.Y. He, L.H. Lu, Dopamine-melanin colloidal nanospheres: an efficient near-infrared photothermal therapeutic agent for in vivo cancer therapy, Adv. Mater. 25 (2013) 1353–1359.
[42] X.C. Li, R. Luo, X.Q. Liang, Q.J. Wu, C.Y. Gong, Recent advances in enhancing reactive oxygen species based chemodynamic therapy, Chin. Chem. Lett. 33 (2022) 2213–2230.
[43] X.Q. Liang, L. Li, X.C. Li, T. He, S.L. Gong, S.Y. Zhu, M.M. Zhang, Q.J. Wu, C. Y. Gong, A spontaneous multifunctional hydrogel vaccine amplifies the innate immune response to launch a powerful antitumor adaptive immune response, Theranostics 11 (2021) 6936–6949.
[44] H.N. Li, J.Y. Sun, H.Y. Zhu, H.X. Wu, H. Zhang, Z.W. Gu, K. Luo, Recent advances in development of dendritic polymer-based nanomedicines for cancer diagnosis, Wiley Interdiscip Rev Nanomed Nanobiotechnol 13 (2) (2021) e1670.
[45] H.N. Li, Y. Feng, Q. Luo, Z.Q. Li, X. Li, H.T. Gan, Z.W. Gu, Q.Y. Gong, K. Luo, Stimuli-activatable nanomedicine meets cancer theranostics, Theranostics 13 (15) (2023) 5386–5417.
[46] L. Gu, Z.Y. Duan, X. Li, X. Li, Y.G. Li, X.L. Li, G. Xu, P. Gao, H. Zhang, Z.W. Gu, J. Chen, Q.Y. Gong, K. Luo, Enzyme-triggered deep tumor penetration of a dual-drug nanomedicine enables an enhanced cancer combination therapy, Bioact. Mater. 26 (2023) 102–115.
[47] M.M. Gubin, M.D. Vesely, Cancer immunoediting in the era of immuno-oncology, clin, Cancer Res. 28 (2022) 3917–3928.
[48] M. Luksza, Z.M. Sethna, L.A. Rojas, J. Lihm, B. Bravi, Y. Elhanati, K. Soares, M. Amisaki, A. Dobrin, D. Hoyos, P. Guasp, A. Zebboudj, R. Yu, A.K. Chandra, T. Waters, Z. Odgerel, J. Leung, R. Kappagantula, A. Makohon-Moore, A. Johns, A. Gill, M. Gigoux, J. Wolchok, T. Merghoub, M. Sadelain, E. Patterson, R. Monasson, T. Mora, A.M. Walczak, S. Cocco, C. Iacobuzio-Donahue, B. D. Greenbaum, V.P. Balachandran, Neoantigen quality predicts immunoediting in survivors of pancreatic cancer, Nature 606 (2022) 389–395.
[49] J.S. O'Donnell, M.W.L. Teng, M.J. Smyth, Cancer immunoediting and resistance to T cell-based immunotherapy, Nat. Rev. Clin. Oncol. 16 (2019) 151–167.
[50] M. von Locquenghien, C. Rozalen, T. Celia-Terrassa, Interferons in cancer immunoediting: sculpting metastasis and immunotherapy response, J. Clin. Invest. 131 (2021) e143296.
[51] M.W.L. Teng, J. Galon, W.H. Fridman, M.J. Smyth, From mice to humans: developments in cancer immunoediting, J. Clin. Invest. 125 (2015) 3338–3346.
[52] J.B. Swann, M.J. Smyth, Immune surveillance of tumors, J. Clin. Invest. 117 (2007) 1137–1146.
[53] R.G. Gupta, F.G. Li, J. Roszik, G. Lizee, Exploiting tumor neoantigens to target cancer evolution: current challenges and promising therapeutic approaches, Cancer Discov. 11 (2021) 1024–1039.
[54] Y. Wu, Z. Zhang, Y. Wei, Z. Qian, X. Wei, Nanovaccines for cancer immunotherapy: current knowledge and future perspectives, Chin. Chem. Lett. 34 (2022) 108098.